



CHALMERS
UNIVERSITY OF TECHNOLOGY

Role of Li-Ion Depletion on Electrode Surface: Underlying Mechanism for Electrodeposition Behavior of Lithium Metal Anode

Downloaded from: <https://research.chalmers.se>, 2021-08-31 11:22 UTC

Citation for the original published paper (version of record):

Xu, X., Liu, Y., Hwang, J. et al (2020)

Role of Li-Ion Depletion on Electrode Surface: Underlying Mechanism for Electrodeposition Behavior of Lithium Metal Anode

Advanced Energy Materials, 10(44)

<http://dx.doi.org/10.1002/aenm.202002390>

N.B. When citing this work, cite the original published paper.

Role of Li-Ion Depletion on Electrode Surface: Underlying Mechanism for Electrodeposition Behavior of Lithium Metal Anode

Xieyu Xu, Yangyang Liu, Jang-Yeon Hwang, Olesya O. Kapitanova,* Zhongxiao Song, Yang-Kook Sun, Aleksandar Matic,* and Shizhao Xiong*

The application of lithium metal as an anode material for next generation high energy-density batteries has to overcome the major bottleneck that is the seemingly unavoidable growth of Li dendrites caused by non-uniform electrodeposition on the electrode surface. This problem must be addressed by clarifying the detailed mechanism. In this work the mass-transfer of Li-ions is investigated, a key process controlling the electrochemical reaction. By a phase field modeling approach, the Li-ion concentration and the electric fields are visualized to reveal the role of three key experimental parameters, operating temperature, Li-salt concentration in electrolyte, and applied current density, on the microstructure of deposited Li. It is shown that a rapid depletion of Li-ions on electrode surface, induced by, e.g., low operating temperature, diluted electrolyte and a high applied current density, is the underlying driving force for non-uniform electrodeposition of Li. Thus, a viable route to realize a dendrite-free Li plating process would be to mitigate the depletion of Li-ions on the electrode surface. The methodology and results in this work may boost the practical applicability of Li anodes in Li metal batteries and other battery systems using metal anodes.

The lithium-ion battery is the currently leading energy storage technology for these applications, but will face severe challenges in meeting the increasing energy density demand as the implementation of new chemistries based on high energy density cathodes^[2] will require new anode materials in order to overcome the limited energy density of graphite with a low specific capacity of 372 mAh g⁻¹.^[3] Lithium metal has an ultra-high theoretical specific capacity (3860 mAh g⁻¹), and the lowest reduction potential (−3.04 V vs standard hydrogen electrode) and is thus considered as a “holy grail” for anode materials for high energy-density battery systems.^[2,4] However, the practical application of Li metal batteries (LMBs) has been held back by a low Coulombic efficiency and safety concerns related to use of Li-metal anodes.^[4a, 5]


1. Introduction

With the socio-economic development in past decades the demand for energy storage has increased with mass applications, including digital products, grid-storage, and electric vehicles.^[1]

In general, the problematic issues of Li-metal anodes can be attributed to two main factors, the preferred electrodeposition resulting in a mossy/dendritic morphology and the high reactivity of Li metal toward common liquid electrolytes generating a solid electrolyte interphase (SEI).^[6] The mossy/dendritic morphology of Li inevitably results in a structural collapse of the electrode with

X. Xu, Dr. O. O. Kapitanova
Faculty of Materials Science
Lomonosov Moscow State University
Leninskie gory 1, Moscow 119991, Russia
E-mail: kapitanova@main.inorg.chem.msu.ru,
olesya.kapitanova@gmail.com

Y. Liu, Prof. Z. Song, Dr. S. Xiong
State Key Laboratory for Mechanical Behavior of Materials
Xi'an Jiaotong University
Xi'an 710049, P. R. China

 The ORCID identification number(s) for the author(s) of this article can be found under <https://doi.org/10.1002/aenm.202002390>.

© 2020 The Authors. Published by Wiley-VCH GmbH. This is an open access article under the terms of the Creative Commons Attribution License, which permits use, distribution and reproduction in any medium, provided the original work is properly cited.

Prof. J.-Y. Hwang
Department of Materials Science and Engineering
Chonnam National University
Buk-gu, Gwangju 61186, Republic of Korea

Dr. O. O. Kapitanova
Center for Photonics and 2D Materials
Moscow Institute of Physics and Technology
9 Institutskiy per., Dolgoprudny, Moscow Region 141701, Russia

Prof. Y.-K. Sun
Department of Energy Engineering
Hanyang University
Seoul 04763, Republic of Korea

Prof. A. Matic, Dr. S. Xiong
Department of Physics
Chalmers University of Technology
Göteborg SE 412 96, Sweden
E-mail: matic@chalmers.se; shizhao.xiong@chalmers.se

DOI: 10.1002/aenm.202002390

inactive, “dead”, Li, and/or the formation of dendrites that penetrate the separator creating internal short-circuit and causing severe thermal runaway of the battery.^[6b] Thus, regulation of electrodeposition behavior of Li to obtain a dense microstructure with minimum porosity is an essential route to improve the Coulombic efficiency and to address safety issues for practical Li-metal anodes.^[7] To realize the goal of dendrite-free Li anode, a plenty of the effective strategies have been developed to tackle the non-uniform electrodeposition of Li during plating/stripping process, including the interphase engineering,^[8] the optimization of electrolytes,^[9] the integrated composite electrode,^[10] the utilization of solid-state electrolyte,^[11] and thermally driven suppression of Li dendrite.^[12] Meanwhile, to reveal the dendrite growth from various aspects like reaction kinetics, mass transport and electrochemical conditions, considerable computational studies were performed by using phase-field, kinetic Monte Carlo and hydrodynamic methods.^[13] To a certain extent, these approaches mitigate the dendritic issues, yet, it is still imperative to unravel the fundamental mechanism for the non-uniform electrodeposition behavior of Li-metal anodes.^[3a]

In principle, the electrodeposition process of Li can be divided into two steps: 1) the mass-transfer process in liquid electrolyte for the motion of Li-ions from the bulk electrolyte to the liquid layer near electrode; and 2) the charge-transfer process for the electrodeposition of the Li-ion to an Li-atom on the electrode surface.^[14] In the case of Li electrodeposition, the mass-transfer process is more sluggish compared to the charge transfer process and thus the electrodeposition rate is controlled by the mass-transfer process.^[15] In particular, the mass-transfer of Li-ions is dominated by their mobility in the diffusion regime of the electrodeposition system, which is quantified by the diffusion coefficients.^[15–16] During the electrochemical process, mass-transfer of Li-ion contributes to 1) the spatial distribution of concentration field near electrode, 2) local Faradic current density caused by flux of Li-ions reaching the electrode surface, and 3) the concentration polarization, which is the crucial factor for the electrodeposition.^[17] Naturally, the mass-transfer of Li-ion in electrolyte is highly dependent on the properties of the electrolyte, such as Li-salt concentration, viscosity and ionic conductivity, as well as the operating conditions, such as working temperature and applied current density. Factors like Li-salt concentration, temperature and applied current density have previously been independently investigated with respect to regulating electrodeposition of Li.^[9c, 9d, 15,18] However, a comprehensive view of how these key factors of the mass transfer process jointly affect the electrodeposition behavior of Li is still lacking.

In this work, the underlying relation between mass transfer of Li-ions and the electrodeposition process is investigated by conducting a systemically designed phase-field modeling study. The electrodeposition behavior of Li on a typical substrate is simulated under various conditions of operation temperature, Li-salt concentration and applied current density. We show that these parameters dictate the distribution of the Li-ion concentration and local current density fields in proximity to the electrode surface and thus steer electrodeposition behavior. Specifically, the depletion of Li-ions on the electrode surface induces the preferred growth of Li and promotes a dendritic morphology. Our results provide guiding principles for regulation of mass-transfer of Li-ions to suppress Li dendrite growth

and the methodology used in this work can be generally applied to other battery systems based on metal anodes to understand and tailor the electrodeposition process.

2. Results

2.1. Mass-Transfer Process of Li-Ion on Electrode

As shown in **Figure 1**, the simple overall electrode, reaction of $\text{Li}^+ + e^- \rightleftharpoons \text{Li}$, is composed of a series of steps including the convection of Li-ion, diffusion of desolvated Li-ion and a reduction to Li-atom.^[14b] From an electrochemical point of view, the kinetics of electrodeposition is determined by the overpotential on the electrode, which can be described by Butler–Volmer equation.^[19] The overpotential can be divided into two parts that are induced by mass-transfer (η_c) and electro-reaction (η_E), respectively. Thus, the local Faradic current density (j_F) on the electrode surface can be expressed as

$$j_F \approx j^0 \exp\left(\frac{\alpha F}{RT}(\eta_E + \eta_c)\right) \approx \varepsilon \exp\left(\frac{\alpha F}{RT} \eta_c\right) \quad (1)$$

where j^0 is the exchange current density of Li^+/Li , α is the charge transfer coefficient for reduction of Li-ion, F is Faraday constant, R is universal gas constant, T is the absolute temperature, and $\varepsilon = j^0 \exp\left(\frac{\alpha F}{RT} \eta_E\right)$ is related to the electrochemical polarization.^[20] As previously reported, the reduction of Li-ions on the electrode has relatively fast electrochemical kinetics, and thus the reaction rate is controlled by the rate of mass-transfer.^[21] The mass-transfer of Li-ions in the electrolyte can be considered in three different regions: an electric double layer on the electrode surface, a diffusion layer close to the surface, and in the bulk electrolyte (Figure 1). Here, the mass-transfer in the diffusion layer is at focus as it controls the transport of Li-ions from the bulk to electrode surface.^[22]

In the diffusion layer, the mass-transfer process can be described by Fick’s Second Law

$$\frac{\partial C_{\text{Li}^+}(x,t)}{\partial t} = D_{\text{Li}^+} \frac{\partial^2 C_{\text{Li}^+}(x,t)}{\partial x^2} \quad (2)$$

where $C_{\text{Li}^+}(x,t)$ is the concentration of Li-ions at a certain position (x) above the surface and a certain time (t).^[23] The

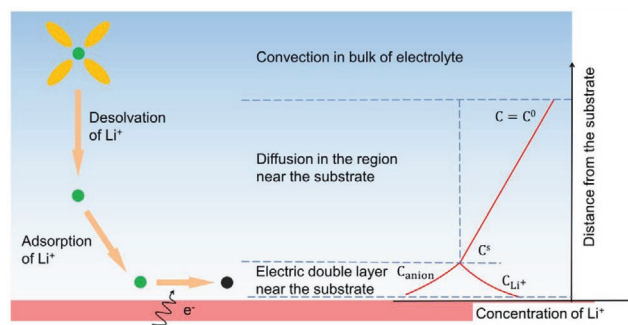


Figure 1. Schematic of mass-transfer of Li-ions and corresponding concentration gradient on the electrode surface.

overpotential induced by mass-transfer can be expressed as the transformed Nernst Equation

$$\eta_c = \frac{RT}{F} \ln \frac{C_{\text{Li}^+}^*}{C_{\text{Li}^+}(0,t)} \quad (3)$$

where $C_{\text{Li}^+}^*$ is the concentration of electrolyte. The overpotential induced by mass transfer in the diffusion layer under galvanostatic conditions can then be written as (see detailed derivation process in the Supporting Information)

$$\eta_c = -\frac{RT}{F} \ln \left(1 - \frac{2j\sqrt{t}}{F\sqrt{\pi D_{\text{Li}^+}}} \right) \quad (4)$$

From the Equation (4), it is clearly seen that the operation temperature (T), applied current density (j), and diffusion coefficient of Li-ion (D_{Li^+}), which are closely associated to the properties of the electrolyte and operation conditions of the cell, are crucial parameters determining the transport of Li-ions near the electrode surface and thus regulating the electrodeposition behavior.

To precisely simulate the electrodeposition process of Li under various conditions, we built a substrate ($6 \times 10 \mu\text{m}^2$) with rectangular pillars ($1 \times 2 \mu\text{m}^2$) (Figure S1, Supporting Information) to mimic a real substrate and the initial morphology of a Li electrode following results in literature shows that the 0D or 1D nucleation of Li induces rod-like or needle-like morphology.^[24] Moreover, regular patterns or frameworks have also been used as substrate to regulate the electrodeposition of Li.^[25] With this substrate as a base, the phase-field modeling was performed

using the COMSOL software to visualize the Li-ion concentration and the electric fields near the substrates and to follow the evolution of deposited Li as a function of time steps.^[26]

2.2. Effect of Operating Temperature on Electrodeposition of Li

The operating temperature determines the diffusion rate of the Li-ion (Table S1, Supporting Information) and thus significantly affects the mass-transfer process near the substrate surface.^[26b] With applied current a concentration gradient is formed in the electrolyte above the electrode surface. With increasing temperature the diffusion rate increases^[18b] and the concentration gradient distinctly decreases (Figure 2a-c). At low temperatures (-30°C) there is a strong depletion of Li-ions ($C < 0.2 \text{ M}$) above the whole electrode surface. With increasing temperature, the gradient is smaller and a relatively homogeneous concentration field is obtained also between pillars on the electrode surface at 50°C . Similarly, the Faradic current density induced by the concentration field between the top and the bottom of the pillars is highly dependent on operation temperature. The Faradic current turns to be 0 between the pillars at low temperature and thus the Li deposition is expected to just occur on the top of the pillars. In other words, high temperature will accelerate mass-transfer kinetics and result in a relatively uniform electrodeposition of Li (Figure S2, Supporting Information).

The electrodeposition process under galvanostatic conditions was followed as a function of time. Initially (10 s of evolution time) (Figure S3, Supporting Information), at -30°C a small hat-like Li layer forms on top of the pillars with negligible

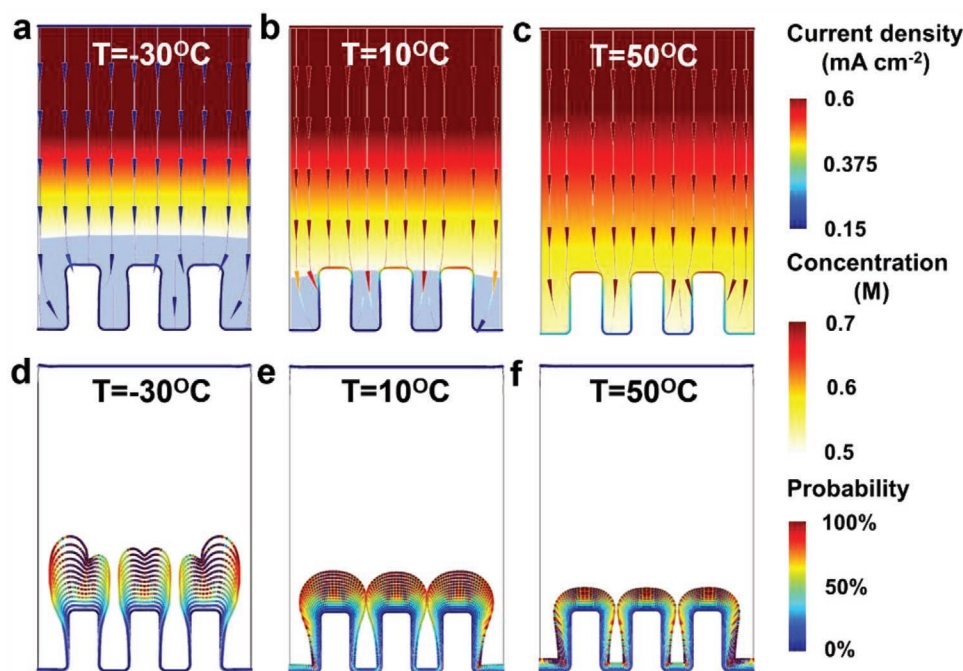


Figure 2. Influence of temperature on Li-ion concentration and electric fields close to the electrode surface and evolution of deposited Li morphology as function of operating temperature a,d) $T = -30^\circ\text{C}$, b,e) $T = 10^\circ\text{C}$ and c,f) $T = 50^\circ\text{C}$. Colored lines in figures (a–c) represent electric field lines, with different intensity, and the background color represents Li-ion concentration, where the light blue region shows strong Li-ion depletion ($<0.2 \text{ M}$). Colored dotted lines in figures (d–f) represents the local electrodeposition probability of Li.

probability for further electrodeposition. At higher temperature, the deposited layer is progressively more homogeneous over the electrode surface with a finite probability for further electrodeposition. The process was followed until coverage of the regions between the pillars was obtained and the evolution of deposited Li morphology is shown in Figure 2d–f. A branched morphology of deposited Li is found at $-30\text{ }^{\circ}\text{C}$ (after $t = 130\text{ s}$), which can potentially develop to a dendritic morphology, and nearly all Li is in this case deposited at the top of the pillars (Figure 2d) as a result of distribution of the Faradic current density shown in Figure S2 (Supporting Information). In contrast, at higher temperature much more uniform distribution of Li is found with a bulb-like morphology of deposited Li (Figure 2e,f) and the time to fill the gap between the pillars is also shorter, $t = 32\text{ s}$ and $t = 18\text{ s}$, respectively (Figure S4, Supporting Information). It is worth noting that the deposited Li at $50\text{ }^{\circ}\text{C}$ covers the pillar from top to bottom with a relatively even thickness layer compared to the deposition at $-30\text{ }^{\circ}\text{C}$. Moreover, the probability of the electrodeposition corresponding to further growth of Li onto the existing morphology is also dependent on the operating temperatures. At the final state of the simulation, Figure S5 (Supporting Information), the high-probability region appears at the top area of the pillars at lower temperatures (-30 and $10\text{ }^{\circ}\text{C}$), while the probability between them is less than 30%. At high temperature ($50\text{ }^{\circ}\text{C}$) a rather even probability is observed over the surface profile indicating that a quasi-homogeneous electrodeposition of Li can be expected. These results clearly show the connection between the mass-transfer kinetics as controlled by temperature and the uniformity of the Faradic current density on substrate. With slow kinetics the Li-ion depletion is severe and electrodeposition of Li

preferentially occurs on top of the pillars and a branched dendritic morphology develops. When the mass transfer of Li-ion is accelerated by elevated temperature, a more uniform electrodeposition of Li with dendrite-free structure can be achieved.

2.3. Effect of Li-Salt Concentration in the Bulk Electrolyte on Electrodeposition of Li

The physicochemical properties of the electrolyte, such as viscosity, density and conductivity, are directly related to the mass transfer of Li-ions.^[27] To investigate the effect of these properties on electrodeposition behavior of Li, we selected tetraethylene glycol dimethyl ether (TEGDME) as solvent and lithium bis(trifluoromethanesulfonyl)imide (LiTFSI) as salt to prepare series of electrolytes with concentrations in the range $0.14\text{--}2.25\text{ m}$. The diffusion coefficients of Li-ion in these electrolytes were calculated with the Einstein–Stokes equation based on the data in Table S2 (Supporting Information) and are shown in Table S3 (Supporting Information).

For a better comparison of the modeling results for the different electrolytes, the concentration field is normalized to the range from 0 to $2C$. The isoconcentration of 0 is moving away from the surface of substrate when the bulk electrolyte concentration decreases from 0.28 to 0.14 m (Figure 3a,b) suggesting that there is a strong Li-ion depletion at the surface and a huge concentration gradient develops. However, in the electrolytes with a Li-salt concentration higher than 0.56 m a much lower concentration gradient is observed and for the highly concentrated electrolyte (2.25 m) there is an even concentration (Figure 3c–e). As a result, for electrolytes with a low

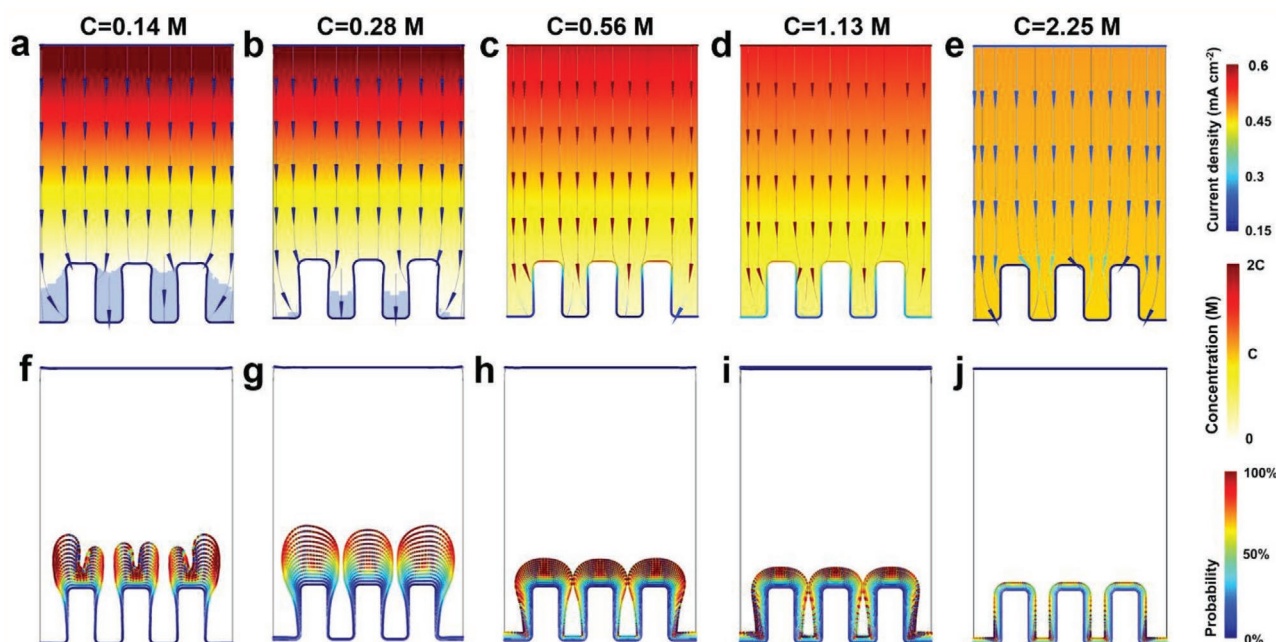


Figure 3. Li-ion concentration and electric fields on the electrode and corresponding electrodeposition of Li in electrolytes with different Li-salt concentration. Concentration and corresponding electric fields on the electrode surface and the evolution of the morphology of deposited Li in electrolytes with Li-salt concentration a,f) $C = 0.14\text{ m}$, b,g) $C = 0.28\text{ m}$, c,h) $C = 0.56\text{ m}$, d,i) $C = 1.13\text{ m}$ and e,j) $C = 2.25\text{ m}$. The definition of colored lines here is the same as that used in Figure 2.

salt concentration (0.14 and 0.28 M) the Faradic current density is low and between the pillars it is close to zero and electro-deposition of Li barely occurs there. When the concentration increases to 0.56 M, the Faradic current density increases and there is an increased difference between the top and the bottom of the pillars (Figure S6, Supporting Information). A decreased Faradic current density is then obtained 1.13 M. It is worth noting that a remarkably uniform distribution of Faradic current density is obtained with the highly concentrated electrolyte (2.25 M), which thus provides conditions for an even electro-deposition of Li.

The evolution of the electro-deposition process is followed in the simulation with the coupled concentration and electric fields. In the dilute electrolytes of (0.14 and 0.28 M) electro-deposition basically only occurs on top of the pillars, as seen in Figure S7 (Supporting Information). At higher electrolyte concentrations a bulb-like morphology is observed and for the highly concentrated electrolyte a strikingly even distribution of deposited Li is found. As the process continues this results in differences in the morphology with electrolyte concentration, from a highly branched morphology for the lowest concentration to a uniform Li layer at the highest concentrations. One should also note that the thickness of the deposited Li layer is higher in the 0.28 M electrolyte compared to the higher concentrations which is a result of a less dense, porous, microstructure being formed. It takes $t = 770$ s, $t = 140$ s, $t = 25$ s, and $t = 20$ s, for the modeling with electrolyte of 0.14, 0.28, 0.56, and 1.13 M, respectively. And a longer time of $t = 38$ s is used to consume, there absent connected Li metal when use electrolyte of 2.25 M (Figure S8, Supporting Information). At the final states of the simulations (Figure S9, Supporting Information) the deposited Li shows a branched or bulb-like morphology in electrolytes with low Li-salt concentration as a result of a higher electric intensity which promotes the progression of growth along these structures. In contrast a fully uniform electro-deposition of Li is observed in the highly concentrated electrolyte (Figure S9e, Supporting Information).

2.4. Effect of Applied Current Density on Electrodeposition of Li

The applied current density is a key factor to determine the overpotential induced by mass transfer of Li-ions, Equation (4), and thus it will also contribute to the local Faradic current density on the electrode surface. A series of current densities, ranging from 0.25 to 50 mA cm⁻², were applied to investigate the effect on the electro-deposition of Li. As shown in Figure 4a-d, the depletion region (<0.2 M) shifts to further away from substrate surface with increasing applied current density up to 2.0 mA cm⁻² and barely moves with a further increase (Figure 4e-h). Specifically, a relatively uniform distribution of local Faradic current density is found on top of the pillars for applied current densities below 5.0 mA cm⁻², whereas a concentration of Faradic current density is found at the corners of the pillars when the applied is further increased (Figures S10, Supporting Information), which will lead to a preferred electro-deposition of Li at this spot.

The evolution of Li deposition as a function of applied current density is shown in Figure 4i-p and Figure S11 (Supporting Information). With increasing applied current density the deposition becomes less uniform and branched morphologies appear at the highest current densities as a result of the variation of the location for the highest probability of electro-deposition with applied current density. For low current density there is a rather uniform probability for deposition over the substrate, while for higher current densities it is considerably higher top of the pillars, in agreement with the distribution of local Faradic current density. This results in a bulb-like morphology at applied current density of 0.25 to 2.0 mA cm⁻² and where the height of Li deposits also increases with larger current density (Figure 4i-l). Above 5 mA cm⁻² a rapid growth on top of the pillars is observed and when the applied current density is up to 10 mA cm⁻² (Figure 4m-p), the morphology of Li shows a highly branched structure indicating that a needle-like Li dendrite morphology will develop. In addition, the height of the deposits increases with the non-uniformity (Figure S12, Supporting Information). This is consistent with the faster deposition (increased thickness) following the relation of $l = \frac{j \times t \times M}{F \times \rho}$ (l : height of dendritic Li, t : deposition time, M : concentration of electrolyte, ρ : density).^[28] The time required to cover the regions between the pillars shows a non-monotonic behavior with applied current density (Figure S13, Supporting Information). In general, it decreases with increasing applied current density but has a local maximum at 5 mA cm⁻². At the final state of modeling (Figure S14, Supporting Information), uniform distribution of deposited Li and probability for deposition are observed for low applied current density while higher applied current density accelerates the electro-deposition process of Li but leads to the branched dendritic morphology.

3. Discussion

Our simulation results demonstrate that elevated operating temperature, highly concentrated electrolytes, and low applied current density are all beneficial to reduce the concentration gradient on the substrate surface, contributing to obtain uniform electro-deposition of Li in a dendrite-free morphology with low porosity. These results are fully in line with the experimental phenomena observations reported in literature, but with a detailed mechanistic explanation.^[29] Here, we link the large concentration gradient, or depletion, of Li-ions on the substrate surface to the electro-deposition process on account of electro-chemical principles and mass-transfer laws. The concentration of Li-ions near substrate can be expressed as (full derivation in the Supporting Information)

$$C_{\text{Li}^+}(0, t) = C_{\text{Li}^+}^* - \frac{2j\sqrt{t}}{F\sqrt{\pi D_{\text{Li}^+}}} \quad (5)$$

in which the diffusion coefficient D_{Li^+} is defined with Stokes-Einstein relation^[30]

$$D_{\text{Li}^+} = \frac{\kappa_B T}{6\pi\eta_d r} \quad (6)$$

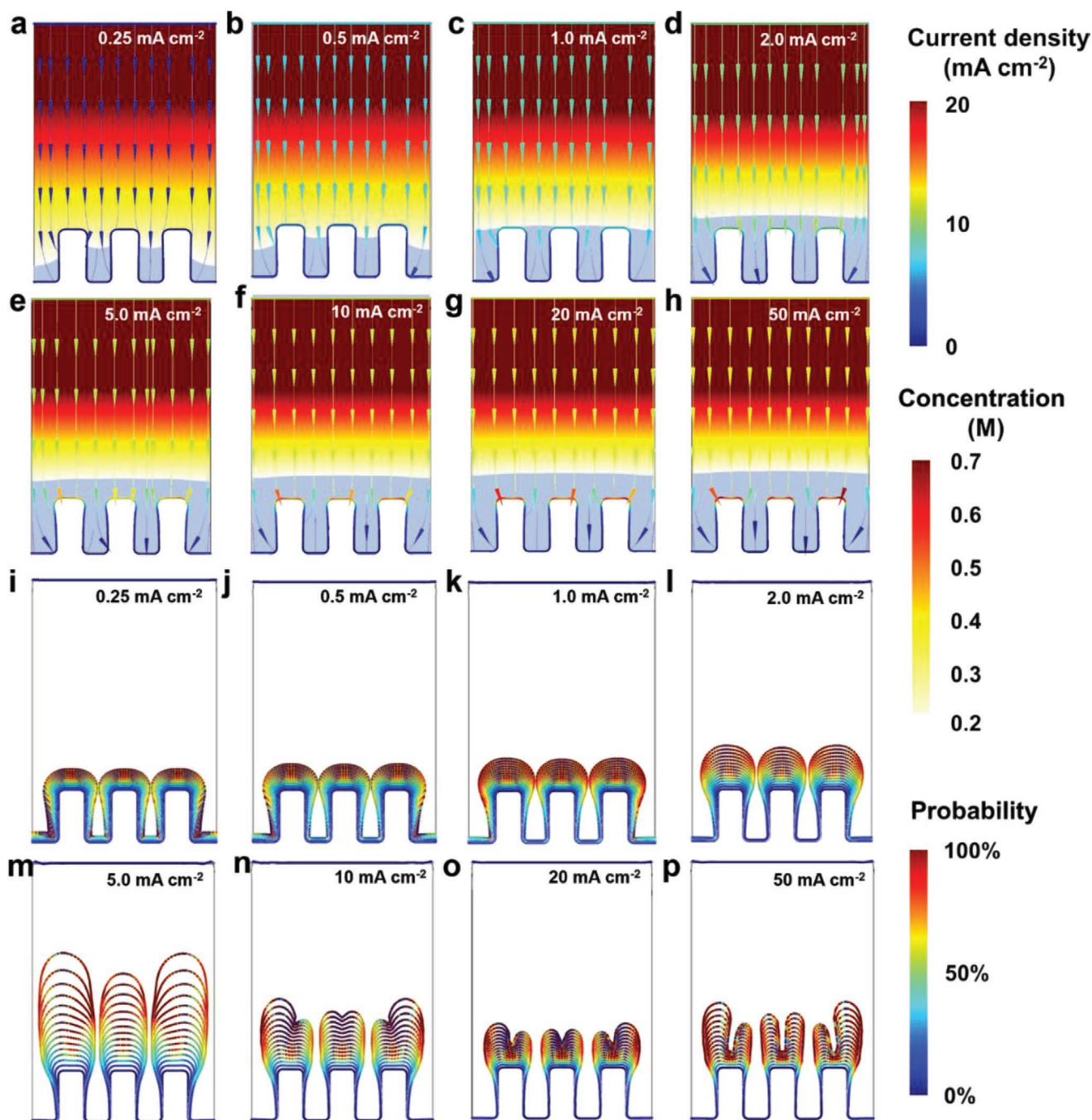


Figure 4. Li-ion concentration and electric fields on electrode and corresponding electrodeposition of Li under different applied current densities. Concentration and electric fields on the electrode surface and the evolution of morphology of deposited Li at current densities a,i) $j = 0.25 \text{ mA cm}^{-2}$, b,j) $j = 0.5 \text{ mA cm}^{-2}$, c,k) $j = 1.0 \text{ mA cm}^{-2}$, d,l) $j = 2.0 \text{ mA cm}^{-2}$, e,m) $j = 5.0 \text{ mA cm}^{-2}$, f,n) $j = 10 \text{ mA cm}^{-2}$, g,o) $j = 20 \text{ mA cm}^{-2}$ and h,p) $j = 50 \text{ mA cm}^{-2}$. The concentration of electrolyte used here is $C = 0.56 \text{ M}$. The definition of colored lines here is the same to that used in Figure 2.

(T : absolute temperatures, η_d : dynamic viscosity, κ_B : Boltzmann's constant, r : radius of Li-ion). Equation (5) can be transformed to

$$\frac{C_{\text{Li}^+}(0,t)}{C_{\text{Li}^+}^*} = 1 - \frac{2j}{FC_{\text{Li}^+}^* \sqrt{\pi D_{\text{Li}^+}}} \sqrt{t} \quad (7)$$

showing the linear relation between surface concentration factor $\frac{C_{\text{Li}^+}(0,t)}{C_{\text{Li}^+}^*}$ and time \sqrt{t} with the slope of $\frac{2j}{FC_{\text{Li}^+}^* \sqrt{\pi D_{\text{Li}^+}}}$.

The slope, determined by the concentration of Li-ions in the bulk electrolyte ($C_{\text{Li}^+}^*$), the Li-ion diffusion coefficient (D_{Li^+}) and the applied current density (j), describes the rate of depletion of Li-ions near the substrate and thus dictates the morphology of

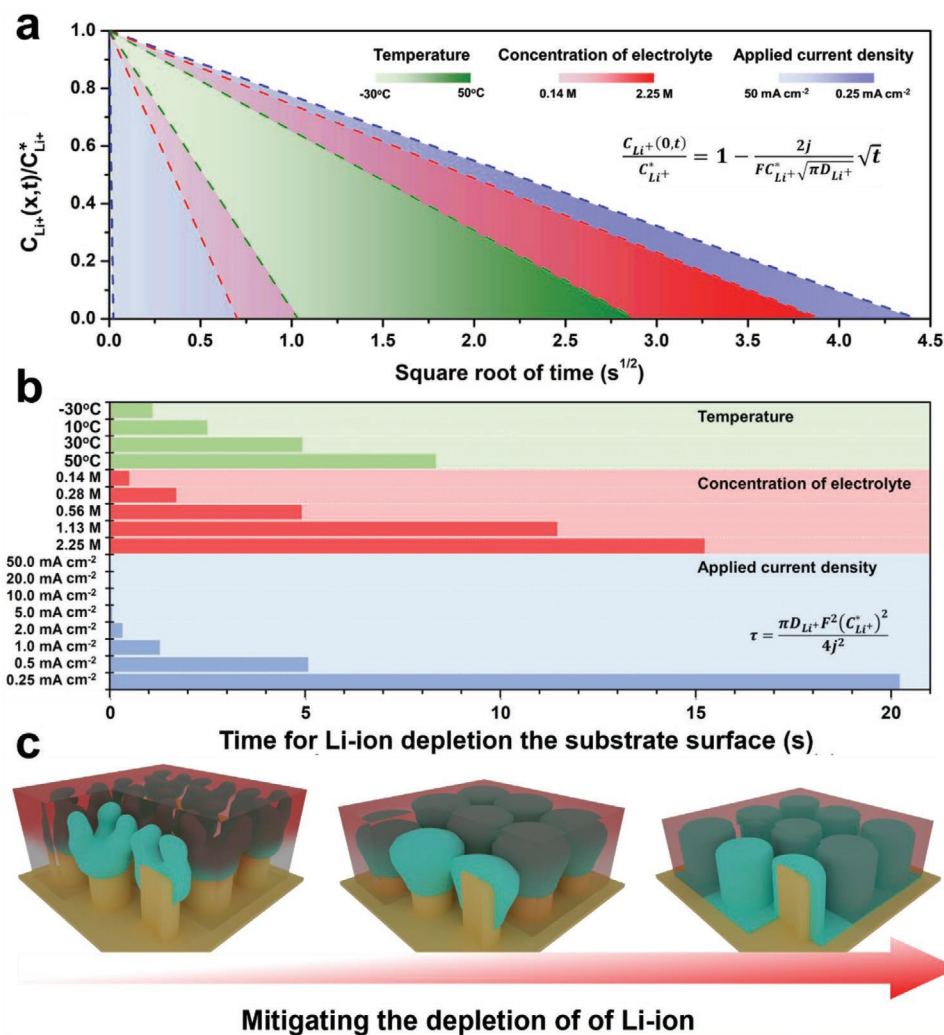


Figure 5. Mitigating the depletion of Li-ion on electrode enables uniform electrodeposition of Li. a) Surface concentration factor as a function of deposition time and b) the time for depletion of Li-ions on the electrode surface under various conditions, including temperature, Li-salt concentration in the electrolyte and applied current density. c) The schematic diagram of depletion of the Li-ions inducing preferred electrodeposition of Li.

deposited Li in the following growth process. The parameters used in the modeling (temperature, Li-salt concentration in the electrolyte and applied current density) are extracted and calculated by Equation (7) (Table S4, Supporting Information)^[28] and in **Figure 5a** the results are plotted by overlapped layers in order to directly compare them. For each parameter, time to depletion of Li-ion on electrode surface shown in **Figure 5b**. This shows that:

- Higher temperature boosts the mobility of Li-ions as a result of the increased diffusion coefficient,^[18b,31] and thus yields smaller slope in **Figure 5a**, increasing the time of depletion on the electrode surface.
- Highly concentrated electrolytes have a higher viscosity which will decrease the mobility of Li-ions,^[32] but its value of $C_{Li^+}^* \sqrt{\pi D_{Li^+}}$ is still high due to the high nominal ion concentration. Therefore, the increase of Li-salt concentration in the electrolyte can ultimately lower the slope and sufficient

concentration of Li-ions can be maintained on electrode surface.

- Smaller applied current density can lower the slope directly due to the reduced consumption rate of Li-ions and thus delay the depletion on the electrode surface (**Figure 5**).

Therefore, we suggest that in designing a strategy lowering the slope in Equation (7) in order to postpone the depletion of Li-ions, that is, to maintain high enough concentration of Li-ions near the electrode surface (**Figure 5c**) is the key to realize uniform electrodeposition of Li with a dense and dendrite free morphology. This result can be further used to optimize experimental deposition conditions for a certain current density. For instance, in order to delay the Li-ion depletion (t is set to 15 s and surface concentration factor is set to 0.5) under a relatively high applied current density ($j = 10 \text{ mA cm}^{-2}$), the range of operating temperature and Li-salt concentration can be determined from $C_{Li^+}^* \sqrt{\pi D_{Li^+}} = 0.0161$ associated with Equation (6).

4. Conclusion

In summary, the effect of mass-transfer on the electrodeposition behavior of Li is comprehensively investigated by phase-field modeling in this work. The role of three crucial parameters impacting mass-transfer of Li-ions near the electrode surface, operating temperature, Li-salt concentration in the electrolyte and applied current density, has been evaluated in the model. We found that a large concentration gradient near the substrate, which can be caused by low temperature, diluted electrolyte, and high applied current density, invariably results in non-uniform distribution of local Faradic current density over a typical substrate. Therefore, preferred electrodeposition of Li at certain locations, such as on top of protrusions and edges, generates a highly branched morphology and even a dendritic microstructure after long-term deposition. Based on the analyses of electrodeposition with tunable parameters in a broad range we suggest that postponing the depletions of Li-ion on the substrate surface is the key to realize uniform electrodeposition. Our finding points out a general design strategy where temperature, electrolyte formulation, and applied current density are balanced to obtain a dense and dendrite free morphology upon Li depletion which is crucial in order to apply Li-metal anodes in next generation high energy-density battery systems.

5. Simulation Section

The deposition process of Li is simulated on a substrate (as seen in Figure S1 (Supporting Information)) under various conditions and the boundary effect is applied in the modeling process. We assume that the deposition efficiency on the anode is 100%, regardless of side reactions or the natural convection in the electrolyte.^[22,33]

The fluxes of anions and cations in the electrolyte are calculated by the Nernst–Planck equation^[34]

$$N_i = -D_i \nabla C_i - z_i u_i F c_i \nabla \phi_i \quad (8)$$

where N_i is the transfer vector ($\text{mol m}^{-2} \text{s}^{-1}$), c_i is the electrolyte concentration (mol m^{-3}), z_i is the number of ionic charge, u_i is the ion mobility ($\text{m}^2 \text{s}^{-1} \text{J}^{-1} \text{mol}^{-1}$), F is the Faraday constant, and ϕ_i is the electrolyte potential (V). Therefore, the mass-transfer equation can be expressed as

$$\frac{\partial c_i}{\partial t} + \nabla \cdot N_i = 0 \quad (9)$$

in which $N_i = 1, 2$ represent cation and anion in the electrolyte solution, respectively. The system is electrically neutral, and the conservation equation is written as below

$$\sum_i z_i c_i = 0 \quad (10)$$

The deposition process is described according to the simplified reaction formula



The local current density is determined by the Butler–Volmer equation as^[26c, 35]

$$i_{\text{ct}} = i_0 \left[\exp\left(\frac{1.5F}{RT} \eta\right) - \exp\left(-\frac{0.5F}{RT} \eta\right) \right] \quad (12)$$

In the above equation, ϕ_{eq} is equilibrium electrode potential, η is overpotential, as defined below

$$\begin{aligned} \phi_{\text{eq}} &= \phi_0 - \frac{RT}{nF} \ln\left(\frac{1}{c_{\text{Li}^+}}\right)^{v_{\text{Li}^+}} \\ \eta &= \phi_{\text{s},0} - \phi_1 - \Delta\phi_{\text{eq}} \end{aligned} \quad (13)$$

where $\phi_{\text{s},0}$ is the potential of the electrode.^[26a, 33a] Therefore, the boundary conditions of the anode can be expressed as

$$N_{\text{Li}^+} \cdot n = -\frac{i_0}{2F} \left[\frac{\exp\left(\frac{1.5F(\phi_{\text{s},\text{an}} - \phi_1 - \Delta\phi_{\text{eq}})}{RT}\right) - \frac{c_{\text{Li}^+}}{c_{\text{Li}^+, \text{ref}}}}{\exp\left(-\frac{0.5F(\phi_{\text{s},\text{an}} - \phi_1 - \Delta\phi_{\text{eq}})}{RT}\right)} \right] \quad (14)$$

where n represents the normal vector of the boundary. The rest of the boundaries are insulating boundaries which are given by the following equation

$$N_{\text{Li}^+} \cdot n = 0 \quad (15)$$

For anions and solvent molecules, the insulation conditions are given at each boundary

$$N_{\text{an,org}} \cdot n = 0 \quad (16)$$

The initial conditions are written as

$$c_{\text{cat}} = c_0, \quad c_{\text{an}} = c_0 \quad (17)$$

The stoichiometric coefficient of Li-ion in the electrolyte is $v_{\text{Li}^+} = -1$, and the stoichiometric coefficient of Li atoms on the electrode is $v_{\text{Li}^+} = 1$.

The phase field model in our work is carried out by finite element method on a COMSOL Multiphysics 5.5 platform. The area of the simulation of local current density on Li electrode is $6 \times 10 \mu\text{m}$. We use implicit Euler method, with a time step of $\Delta t = 0.01 \text{ s}$. To acquire high-quality calculation results, the simulation model is built by using ultra-fine grid division. The maximum grid size of the model is $0.015 \mu\text{m}$ and the deformation of the grid during the deposition process is considered. To obtain the local probability for Li deposition, the volume change of each deformable grid in a unit time is calculated by the Faraday's laws of electrolysis on account of local Li-ion concentration and local current density on the electrode surface. The local probability for grid with the most volume change is defined as 100% and also used as the reference for the calculation on remaining grids.

Supporting Information

Supporting Information is available from the Wiley Online Library or from the author.

Acknowledgements

X.X. and Y.L. contributed equally to this work. The work is supported by the Swedish Foundation for International Cooperation in Research and Higher Education (STINT) and the Chalmers Areas of Advance Materials Science and Energy. The authors thank the National Natural Science Foundation of China (No. 51802256) and China Scholarship Council (No. 201908090043) for supporting this work. The authors acknowledge the support from the 111 Project 2.0 (BP2018008).

Conflict of Interest

The authors declare no conflict of interest.

Keywords

depletion of Li-ions, electrodeposition, lithium metal anodes, mass-transfer, surface concentration

Received: July 24, 2020

Revised: September 28, 2020

Published online: October 13, 2020

- [1] D. Larcher, J. M. Tarascon, *Nat. Chem.* **2015**, *7*, 19.
- [2] P. G. Bruce, S. A. Freunberger, L. J. Hardwick, J. M. Tarascon, *Nat. Mater.* **2012**, *11*, 19.
- [3] a) J. Liu, Z. N. Bao, Y. Cui, E. J. Dufek, J. B. Goodenough, P. Khalifah, Q. Y. Li, B. Y. Liaw, P. Liu, A. Manthiram, Y. S. Meng, V. R. Subramanian, M. F. Toney, V. V. Viswanathan, M. S. Whittingham, J. Xiao, W. Xu, J. H. Yang, X. Q. Yang, J. G. Zhang, *Nat. Energy* **2019**, *4*, 180; b) N. Nitta, F. Wu, J. T. Lee, G. Yushin, *Mater. Today* **2015**, *18*, 252; c) X. Jiao, Y. Liu, B. Li, W. Zhang, C. He, C. Zhang, Z. Yu, T. Gao, J. Song, *Carbon* **2019**, *148*, 518.
- [4] a) D. Lin, Y. Liu, Y. Cui, *Nat. Nanotechnol.* **2017**, *12*, 194; b) B. Liu, J.-G. Zhang, W. Xu, *Joule* **2018**, *2*, 833.
- [5] X. B. Cheng, R. Zhang, C. Z. Zhao, Q. Zhang, *Chem. Rev.* **2017**, *117*, 10403.
- [6] a) K. N. Wood, M. Noked, N. P. Dasgupta, *ACS Energy Lett.* **2017**, *2*, 664; b) S. S. Zhang, *ACS Appl. Energy Mater.* **2018**, *1*, 910; c) C. Fang, J. Li, M. Zhang, Y. Zhang, F. Yang, J. Z. Lee, M. H. Lee, J. Alvarado, M. A. Schroeder, Y. Yang, B. Lu, N. Williams, M. Ceja, L. Yang, M. Cai, J. Gu, K. Xu, X. Wang, Y. S. Meng, *Nature* **2019**, *572*, 511.
- [7] S. Jiao, J. Zheng, Q. Li, X. Li, M. H. Engelhard, R. Cao, J.-G. Zhang, W. Xu, *Joule* **2018**, *2*, 110.
- [8] a) Y. C. Yin, Q. Wang, J. T. Yang, F. Li, G. Zhang, C. H. Jiang, H. S. Mo, J. S. Yao, K. H. Wang, F. Zhou, H. X. Ju, H. B. Yao, *Nat. Commun.* **2020**, *11*, 1761; b) Y. M. Zhao, G. X. Li, Y. Gao, D. W. Wang, Q. Q. Huang, D. H. Wang, *ACS Energy Lett.* **2019**, *4*, 1271; c) Y. Liu, X. Xu, X. Jiao, L. Guo, Z. Song, S. Xiong, J. Song, *Chem. Eng. J.* **2019**, *371*, 294; d) Y. Liu, S. Xiong, J. Deng, X. Jiao, B. Song, M. Aleksandar, J. Song, *Sci. China Mater.* **2020**, *63*, 1036.
- [9] a) J. Holoubek, M. Yu, S. Yu, M. Li, Z. Wu, D. Xia, P. Bhaladhare, M. S. Gonzalez, T. A. Pascal, P. Liu, Z. Chen, *ACS Energy Lett.* **2020**, *5*, 1438; b) L. Xiao, Z. Zeng, X. Liu, Y. Fang, X. Jiang, Y. Shao, L. Zhuang, X. Ai, H. Yang, Y. Cao, J. Liu, *ACS Energy Lett.* **2019**, *4*, 483; c) J.-Y. Hwang, S.-J. Park, C. S. Yoon, Y.-K. Sun, *Energy Environ. Sci.* **2019**, *12*, 2174; d) H. Lee, J.-Y. Hwang, J. Ming, Z. Cao, H. A. Nguyen, H.-G. Jung, J. Kim, Y.-K. Sun, *Adv. Energy Mater.* **2020**, *10*, 2000567.
- [10] a) Q. Li, S. Zhu, Y. Lu, *Adv. Funct. Mater.* **2017**, *27*, 1606422; b) S.-S. Chi, Y. Liu, W.-L. Song, L.-Z. Fan, Q. Zhang, *Adv. Funct. Mater.* **2017**, *27*, 1700348; c) L. Fan, S. Li, L. Liu, W. Zhang, L. Gao, Y. Fu, F. Chen, J. Li, H. L. Zhuang, Y. Lu, *Adv. Energy Mater.* **2018**, *8*, 1802350.
- [11] a) S. Xiong, Y. Liu, P. Jankowski, Q. Liu, F. Nitze, K. Xie, J. Song, A. Matic, *Adv. Funct. Mater.* **2020**, *30*, 2001444; b) A. Manthiram, X. Yu, S. Wang, *Nat. Rev. Mater.* **2017**, *2*, 16103; c) Q. Liu, D. Zhou, D. Shanmukaraj, P. Li, F. Kang, B. Li, M. Armand, G. Wang, *ACS Energy Lett.* **2020**, *5*, 1456; d) F. Zhao, Q. Sun, C. Yu, S. Zhang, K. Adair, S. Wang, Y. Liu, Y. Zhao, J. Liang, C. Wang, X. Li, X. Li, W. Xia, R. Li, H. Huang, L. Zhang, S. Zhao, S. Lu, X. Sun, *ACS Energy Lett.* **2020**, *5*, 1035.
- [12] a) L. Li, S. Basu, Y. Wang, Z. Chen, P. Hundekar, B. Wang, J. Shi, Y. Shi, S. Narayanan, N. Koratkar, *Science* **2018**, *359*, 1513; b) B. S. Vishnugopi, F. Hao, A. Verma, P. P. Mukherjee, *ACS Appl. Mater. Interfaces* **2020**, *12*, 23931; c) Z. Hong, V. Viswanathan, *ACS Energy Lett.* **2019**, *4*, 1012.
- [13] a) G. Yoon, S. Moon, G. Ceder, K. Kang, *Chem. Mater.* **2018**, *30*, 6769; b) J. Tan, A. Cannon, E. Ryan, *J. Power Sources* **2020**, *463*, 228187; c) B. S. Vishnugopi, A. Verma, P. P. Mukherjee, *J. Phys. Chem. C* **2020**, *124*, 16784; d) A. Aryanfar, T. Cheng, A. J. Colussi, B. V. Merinov, W. A. Goddard, 3rd, M. R. Hoffmann, *J. Chem. Phys.* **2015**, *143*, 134701; e) Z. Hong, V. Viswanathan, *ACS Energy Lett.* **2018**, *3*, 1737; f) B. S. Vishnugopi, F. Hao, A. Verma, P. Mukherjee, *Phys. Chem. Chem. Phys.* **2020**, *22*, 11286.
- [14] a) P. Biswal, S. Stalin, A. Kludze, S. Choudhury, L. A. Archer, *Nano Lett.* **2019**, *19*, 8191; b) X. R. Chen, Y. X. Yao, C. Yan, R. Zhang, X. B. Cheng, Q. Zhang, *Angew. Chem., Int. Ed. Engl.* **2020**, *59*, 7743.
- [15] P. Bai, J. Li, F. R. Brushett, M. Z. Bazant, *Energy Environ. Sci.* **2016**, *9*, 3221.
- [16] M. Park, X. Zhang, M. Chung, G. B. Less, A. M. Sastry, *J. Power Sources* **2010**, *195*, 7904.
- [17] M. E. Hyde, R. G. Compton, *J. Electroanal. Chem.* **2003**, *549*, 1.
- [18] a) D. Rehnlund, C. Ihrfors, J. Maibach, L. Nyholm, *Mater. Today* **2018**, *21*, 1010; b) Y. Han, Y. Jie, F. Huang, Y. Chen, Z. Lei, G. Zhang, X. Ren, L. Qin, R. Cao, S. Jiao, *Adv. Funct. Mater.* **2019**, *29*, 1904629; c) M. Genovese, A. J. Louli, R. Weber, C. Martin, T. Taskovic, J. R. Dahn, *J. Electrochem. Soc.* **2019**, *166*, A3342; d) X. Dong, Y. Lin, P. Li, Y. Ma, J. Huang, D. Bin, Y. Wang, Y. Qi, Y. Xia, *Angew. Chem., Int. Ed. Engl.* **2019**, *58*, 5623; e) A. Mistry, C. Fear, R. Carter, C. T. Love, P. P. Mukherjee, *ACS Energy Lett.* **2019**, *4*, 156; f) X. Fan, L. Chen, O. Borodin, X. Ji, J. Chen, S. Hou, T. Deng, J. Zheng, C. Yang, S. C. Liou, K. Amine, K. Xu, C. Wang, *Nat. Nanotechnol.* **2018**, *13*, 715.
- [19] J. K. Nørskov, T. Bligaard, A. Logadottir, J. R. Kitchin, J. G. Chen, S. Pandalov, U. Stimming, *J. Electrochem. Soc.* **2005**, *152*, J23.
- [20] A. Jana, S. I. Woo, K. S. N. Vikrant, R. E. García, *Energy Environ. Sci.* **2019**, *12*, 3595.
- [21] J. Lopez, A. Pei, J. Y. Oh, G. N. Wang, Y. Cui, Z. Bao, *J. Am. Chem. Soc.* **2018**, *140*, 11735.
- [22] J. Chalazviel, *Phys. Rev. A* **1990**, *42*, 7355.
- [23] a) C. Monroe, J. Newman, *J. Electrochem. Soc.* **2003**, *150*, A1377; b) J. Philibert, *Diffus. Fundam.* **2005**, *2*, 1.1.
- [24] a) M. Jackle, A. Gross, *J. Chem. Phys.* **2014**, *141*, 174710; b) C. Ling, D. Banerjee, M. Matsui, *Electrochim. Acta* **2012**, *76*, 270.
- [25] a) Y. Li, J. Jiao, J. Bi, X. Wang, Z. Wang, L. Chen, *Nano Energy* **2017**, *32*, 241; b) C. Jin, O. Sheng, J. Luo, H. Yuan, C. Fang, W. Zhang, H. Huang, Y. Gan, Y. Xia, C. Liang, J. Zhang, X. Tao, *Nano Energy* **2017**, *37*, 177; c) J. Park, D. Kim, D. Jin, C. Phatak, K. Y. Cho,

- Y.-G. Lee, S. Hong, M.-H. Ryou, Y. M. Lee, *J. Power Sources* **2018**, 408, 136; d) R. Zhang, X. Chen, X. Shen, X.-Q. Zhang, X.-R. Chen, X.-B. Cheng, C. Yan, C.-Z. Zhao, Q. Zhang, *Joule* **2018**, 2, 764.
- [26] a) L. Chen, H. W. Zhang, L. Y. Liang, Z. Liu, Y. Qi, P. Lu, J. Chen, L.-Q. Chen, *J. Power Sources* **2015**, 300, 376; b) R. Zhang, X. Shen, X.-B. Cheng, Q. Zhang, *Energy Storage Mater.* **2019**, 23, 556; c) Y. Okajima, Y. Shibuta, T. Suzuki, *Comput. Mater. Sci.* **2010**, 50, 118.
- [27] L. Aguilera, S. Xiong, J. Scheers, A. Matic, *J. Mol. Liq.* **2015**, 210, 238.
- [28] K. Nishikawa, T. Mori, T. Nishida, Y. Fukunaka, M. Rosso, T. Homma, *J. Electrochem. Soc.* **2010**, 157, A1212.
- [29] a) X. Zhang, Y. Yang, Z. Zhou, *Chem. Soc. Rev.* **2020**, 49, 3040; b) J. Wang, W. Huang, A. Pei, Y. Li, F. Shi, X. Yu, Y. Cui, *Nat. Energy* **2019**, 4, 664; c) Q. Pang, A. Shyamsunder, B. Narayanan, C. Y. Kwok, L. A. Curtiss, L. F. Nazar, *Nat. Energy* **2018**, 3, 783; d) S. H. Jiao, X. D. Ren, R. G. Cao, M. H. Engelhard, Y. Z. Liu, D. H. Hu, D. H. Mei, J. M. Zheng, W. G. Zhao, Q. Y. Li, N. Liu, B. D. Adams, C. Ma, J. Liu, J. G. Zhang, W. Xu, *Nat. Energy* **2018**, 3, 739; e) X. Xu, D. Zhou, X. Qin, K. Lin, F. Kang, B. Li, D. Shanmukaraj, T. Rojo, M. Armand, G. Wang, *Nat. Commun.* **2018**, 9, 3870; f) L. Suo, Y. S. Hu, H. Li, M. Armand, L. Chen, *Nat. Commun.* **2013**, 4, 1481; g) B. D. Adams, J. Zheng, X. Ren, W. Xu, J.-G. Zhang, *Adv. Energy Mater.* **2018**, 8, 1702097; h) C. P. Yang, Y. X. Yin, S. F. Zhang, N. W. Li, Y. G. Guo, *Nat. Commun.* **2015**, 6, 8058; i) S. Huang, W. Zhang, H. Ming, G. Cao, L. Z. Fan, H. Zhang, *Nano Lett.* **2019**, 19, 1832.
- [30] A. Einstein, *Ann. Phys.* **1905**, 322, 549.
- [31] M. Ishikawa, M. Kanemoto, M. Morita, *J. Power Sources* **1999**, 81–82, 217.
- [32] a) C. m. Comminges, R. Barhdadi, M. Laurent, M. Troupel, *J. Chem. Eng. Data* **2006**, 51, 680; b) M. S. Kilic, M. Z. Bazant, A. Ajdari, *Physical Review E* **2007**, 75, 021503.
- [33] a) E. Mattsson, J. O. M. Bockris, *Trans. Faraday Soc.* **1959**, 55, 1586; b) D. R. Ely, A. Jana, R. E. García, *J. Power Sources* **2014**, 272, 581; c) X.-l. Dong, H. Xing, K.-r. Weng, H.-l. Zhao, *J. Iron Steel Res. Int.* **2017**, 24, 865; d) P. P. Natsiavas, K. Weinberg, D. Rosato, M. Ortiz, *J. Mech. Phys. Solids* **2016**, 95, 92.
- [34] a) J. A. Del Rio, S. Whitaker, *Sci. Rep.* **2016**, 6, 35211; b) V. M. Aguilera, S. Mafé, J. Pellicer, *Electrochim. Acta* **1987**, 32, 483.
- [35] A. V. Sokirko, F. H. Bark, *Electrochim. Acta* **1995**, 40, 1983.